ACS APPLIED ENERGY MATERIALS
Cite This: ACS Appl. Energy Mater. 2019, 2, 6043−6050
Article
www.acsaem.org

Au-MoS_2 Hybrids as Hydrogen Evolution Electrocatalysts

Ronen Bar-Ziv,[†] Priyadarshi Ranjan,[‡] Anna Lavie,[§] Akash Jain,[∥] Somenath Garai,[§,▲] Avraham Bar Hen,[‡] Ronit Popovitz-Biro,[§] Reshef Tenne,[§] Raul Arenal,[⊥,#,▽] Ashwin Ramasubramaniam,*[,○] Luc Lajaunie,*[,▽,◆] and Maya Bar-Sadan*[,‡]

[†]Nuclear Research Center Negev, Beer-Sheva 84190, Israel
[‡]Department of Chemistry, Ben-Gurion University of the Negev, Beer-Sheva 84105, Israel
[§]Department of Materials and Interfaces, Weizmann Institute, Rehovot 76100, Israel
[∥]Department of Chemical Engineering, University of Massachusetts, Amherst, Massachusetts 01003, United States
[⊥]Laboratorio de Microscopías Avanzadas, Instituto de Nanociencia de Aragón, Universidad de Zaragoza, 50018 Zaragoza, Spain
[#]ARAID Foundation, 50018 Zaragoza, Spain
[▽]Instituto de Ciencias de Materiales de Aragon, CSIC—Universidad de Zaragoza, Calle Pedro Cerbuna 12, 50009 Zaragoza, Spain
[○]Department of Mechanical and Industrial Engineering, University of Massachusetts, Amherst, Massachusetts 01003, United States

Supporting Information

ABSTRACT: Core−shell nanoparticles provide a unique morphology to exploit electronic interactions between dissimilar materials, conferring upon them new or improved functionalities. MoS_2 is a layered transition-metal disulfide that has been studied extensively for the hydrogen evolution reaction (HER) but still suffers from low electrocatalytic activity due to its poor electronic conductivity. To understand the fundamental aspects of the MoS_2−Au hybrids with regard to their electrocatalytic activity, a single to a few layers of MoS_2 were deposited over Au nanoparticles via a versatile procedure that allows for complete encapsulation of Au nanoparticles of arbitrary geometries. High-resolution transmission electron microscopy of the Au@MoS_2 nanoparticles provides direct evidence for the core−shell morphology and also reveals the presence of morphological defects and irregularities in the MoS_2 shell that are known to be more active for HER than the pristine MoS_2 basal plane. Electrochemical measurements show a significant improvement in the HER activity of Au@MoS_2 nanoparticles relative to freestanding MoS_2 or Au-decorated MoS_2. The best electrochemical performance was demonstrated by the Au nanostars—the largest Au core employed here—encapsulated in a MoS_2 shell. Density-functional theory calculations show that charge transfer occurs from the Au to the MoS_2 layers, producing a more conductive catalyst layer and a better electrode for electrochemical HER. The strategies to further improve the catalytic properties of such hybrid nanoparticles are discussed.

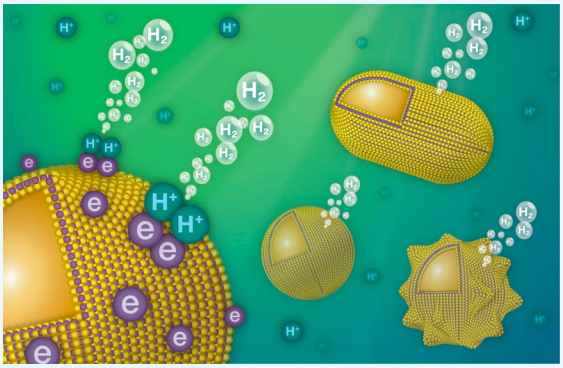

KEYWORDS: *core−shell, density-functional theory, charge transfer, nanostars, nanorods, electrocatalysis, transition-metal dichalcogenides*

1. INTRODUCTION

Layered transition-metal dichalcogenides (TMDs), in particular of Group VIB TMDs such as MoS_2, WS_2, and $MoSe_2$, used traditionally in petrochemistry, have begun to attract interest for key sustainable-energy reactions such as hydrogen evolution reaction (HER) and CO_2 reduction.[1−5] In their ground state (2H phase), Mo and W TMDs are semiconductors with thickness-dependent band-gaps in the range of 1−2 eV[6] and, consequently, are not particularly effective as electrocatalysts. Another limitation of these materials for electrocatalysis, as shown by both calculations and experiments, is that the active sites for HER are located along the (limited) exposed edges while the basal planes are relatively inert. It is against this background that efforts are currently being dedicated to further modify the MoS_2 structures with the aim of improving performance by increasing the density of their catalytic sites by creating defects,[7−9] modifying the morphology, or by doping with other transition metals.[2,3,10,11] Another approach is to combine MoS_2 with other materials and produce hybrids with improved electrical conductivity,[12] more active basal planes,[13] or improved photocatalytic activity.[14,15] Recently, a study exploring the thickness depend-

Received: June 12, 2019
Accepted: August 2, 2019
Published: August 2, 2019

DOI: 10.1021/acsaem.9b01147
ACS Appl. Energy Mater. 2019, 2, 6043−6050

ence (number of layers) of MoS_2 electrocatalysts showed a significant improvement in the catalytic activity for HER with decreasing number of layers.[16] The layer-dependent electrocatalysis was correlated to interlayer hopping of electrons between layers of MoS_2. Therefore, increasing the hopping efficiency is a crucial factor for the design of MoS_2 with optimal catalytic activity. Although many materials have been tested and researched as heterogeneous catalysts, the use of hybrid materials, such as core−shell structures, is a noteworthy approach for tuning the catalytic properties of layered nanomaterials. In particular, increasing evidence shows that the core is not merely an inert support for the shell and complex interactions (electronic and mechanical) at the core−shell interface can alter catalytic behavior at the surface of few-layer shells.[14,17,18] However, there is lesser knowledge about the influence of such core−shell interactions on the mechanisms of electrocatalytic reactions, which is the focus of this work.

Hybrid nanoparticles made of coinage-metal cores coated with MoS_2 layers have been reported recently by several groups.[12,14,15,17,19,20] The choice of Au as a *model* core material, albeit expensive as a practical catalyst, is quite straightforward in this context: Au is inert toward oxidation; Au interacts strongly with MoS_2 via the S atoms; and the localized surface plasmon frequency of nanostructured Au is strong and in the visible range. The optical characteristics of transition-metal core−MoS_2 shell nanoparticles present a new hybridized state between the surface plasmons of the metal core and the exitonic transitions of the MoS_2 shell.[14,15,17] These hybridized states can be optically tuned by varying the shape of the nanoparticles.[21] Further modulation of this transition by coupling to the excitonic modes of MoS_2 has been demonstrated,[14,15,17] offering myriad potential applications.[22] It is therefore appealing to study hybrid Au-MoS_2 core−shell structures as model photocatalysts[23−25] and electrocatalysts.[26] However, while photocatalysis using plasmonic nanostructures is a complex process, wherein a correct understanding of the process may be hindered by strong thermal effects from the metal nanoparticles,[27] electrocatalysis is a more straightforward route toward understanding the basic mechanisms of reactions at Au-MoS_2 surfaces.

In this work, various MoS_2 and Au structures were produced: three geometries of Au cores coated by a conformal MoS_2 shell, as well as a complementary structure consisting of freestanding MoS_2 nanoflowers decorated with exposed Au nanoparticles. All materials were processed to produce drop-casted electrodes from a suspension of the catalysts in a Nafion-based ink, and their electrocatalytic activity toward hydrogen evolution was studied. Electrochemical measurements reveal that the structures with the largest Au core (Au nanostars) are superior HER electrocatalysts with lower onset potentials and Tafel slopes relative to Au-decorated freestanding MoS_2. Density-functional theory (DFT) calculations suggest that the dominant mechanism for the improved catalytic activity is most likely one wherein the Au support promotes the formation of basal-plane S vacancies in MoS_2 and further stabilizes H adsorption at these catalytically active sites. These effects are driven by electron transfer from the Au core to the MoS_2 shell (also seen in the XPS measurements), and such charge transfer could also potentially improve the conductivity of the semiconducting 2H phase, thereby benefiting overall electrocatalytic performance.

2. EXPERIMENTAL SECTION

2.1. Experimental Procedures. All Au cores were preformed and then encapsulated within MoS_2 by overnight stirring with ammonium tetrathiomolybdate ($(NH_4)_2MoS_4$) to bind MoS_4^{-2} anions to the Au cores, using procedures similar to those reported in our previous publication.[17] Detailed procedures for the synthesis of the Au cores, the encapsulation in MoS_2 and the experimental procedures for the preparation of electrodes for the electrocatalytic measurements are available in the Supporting Information. In addition, two reference samples were produced—freestanding MoS_2 and freestanding MoS_2 decorated with Au nanoparticles; detailed synthesis protocols and characterization are provided in the Supporting Information.

2.2. Computational Methods. DFT calculations were performed using Vienna ab Initio Simulation Package (VASP; version 5.4.1).[28,29] The projector-augmented wave (PAW)[30,31] method was used to describe core and valence electrons along with the Perdew−Burke−Ernzerhof (PBE) form[32] of the generalized-gradient approximation to describe electron exchange and correlation. The plane wave kinetic energy cutoff was set to 400 eV, and Gaussian smearing of 0.05 eV was used for Brillouin-zone integrations. Structural optimization was performed using the conjugate-gradient method with a force tolerance of 0.01 eV/Å. The relaxed lattice parameters for bulk Au (FCC) and single-layer MoS_2 (2H phase) are 4.15 and 3.18 Å, respectively. All calculations of isolated MoS_2 were performed using a 4×4 supercell; for Au-supported cases, supercells and atomic positions are provided in the Supporting Information. During relaxation of the MoS_2/Au slab, the bottom two layers of Au were fixed at their bulk positions. To avoid spurious interactions with the periodic images, at least 10 Å of vacuum was inserted normal to the slabs. The Brillouin zone was sampled using a $5 \times 5 \times 1$ Γ-centered *k*-point mesh in all calculations. H-adsorption energies were calculated by inserting one H atom on the surface of the slab, and dipole corrections[33,34] were applied along the normal direction. Electronic density-of-states were calculated using 3000 energy-grid points. Similar to prior studies,[35,36] solvent effects have been neglected here, as a first approximation, and are not expected to change the overall conclusions.

3. RESULTS AND DISCUSSION

The comparative study presented here is based on various morphologies of Au—spherical nanoparticles, elongated nanorods, and spiky Au nanostars—encapsulated within a few MoS_2 layers. In addition, a sample of Au nanoparticles deposited on nanostructured MoS_2 was produced, to represent samples where the Au is directly exposed to the surrounding medium and can itself potentially catalyze the HER reaction.

3.1. Materials Analysis and Characterization with Electron Microscopy. *3.1.1. Gold Particles Embedded within MoS_2 (P-Au@MoS_2).* Similar to the prior work,[17] the product consisted of nanoparticles with sizes between 10 and 20 nm embedded within almost amorphous material. Figure 1a shows a TEM image of an assortment of P-Au@MoS_2 nanostructures showing that the Au cores are sheathed conformably by MoS_2 monolayers (blue arrows in Figure 1d); often, this core−shell morphology is seen more clearly at higher magnification in Figure 1b. Figure S1 shows the core level EELS spectrum of one such nanoparticle, showing Au, Mo, and S signals. Figure 1c shows a STEM HAADF image of a group of P-Au@MoS_2 nanoparticles while Figure 1d displays a single nanoparticle at higher magnification using the same technique. Automatic indexing of the FFT performed using the JEMS software[37] revealed that the core of the nanoparticle corresponds to the Au face-centered cubic structure seen along the [011] zone axis. The Au core forms a multiply twinned particle, typical of Au nanostructures, with a truncated octahedron morphology.

DOI: 10.1021/acsaem.9b01147
ACS Appl. Energy Mater. 2019, 2, 6043−6050

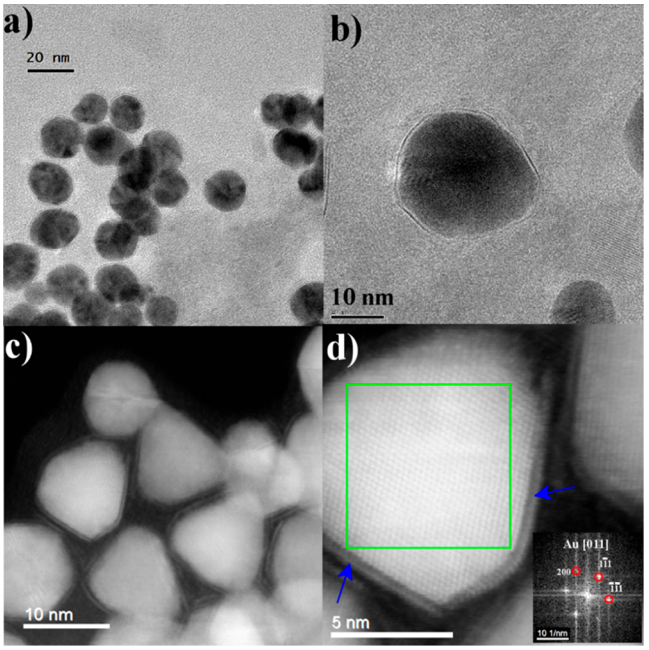

Figure 1. Electron microscopy images of P-Au@MoS_2. (a) TEM image of a few particles. (b) TEM image of a single particle. (c) STEM HAADF image of a group of particles with truncated-tetrahedron Au core structure. (d) HR-STEM HAADF of a single particle. The inset shows the FFT analysis performed at the center of the nanoparticle in the area highlighted by the green square.

3.1.2. Gold Rods Embedded within MoS_2 (R-Au@MoS_2). The Au nanorods (aspect ratio of ~3), were coated with MoS_2 forming a single layer (Figure 2a) or a few-layers thick coating

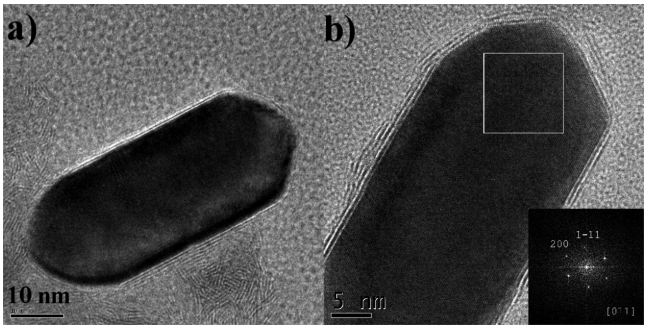

Figure 2. (a, b) TEM image of an individual gold nanorod within MoS_2 (R-Au@MoS_2). The inset in panel b shows the FFT analysis performed within the area highlighted by the gray square.

(Figure 2b), embedded within MoS_2 amorphous material. The coating of the MoS_2 layer was not as perfect as that for the spherical nanoparticles,[17] frequently consisting of incomplete shells. The Fourier transform (FFT) within the inset of Figure 2b shows the reflections from the (200) and ($1\bar{1}1$) planes of Au. Note that the Au lattice is not coincident with the growth axis in this case. Figure S2 shows another Au nanorod coated with a monolayer of MoS_2: the perfect contour of the MoS_2 layer and the lattice image of the Au nanorod can be appreciated. The (001) plane of the Au lattice is parallel to the growth axis of the nanorod, which is not always the case (vide infra). It is nonetheless not clear at this point if the lattice of the Au nanorod has any influence on the growth mode of the top MoS_2 layer. Figure S3 shows a tilt series of one such nanorod in three angles (0, ±25°). The tilt series shows, that, notwithstanding the imperfections in the MoS_2 layer, it encapsulates the entire Au nanorod. Note that the hybrid nanoparticle was placed on a lacy grid with its upper part placed on the amorphous carbon frame and its lower part suspended in vacuum. Therefore, the contrast and image quality of the MoS_2 layer placed on the amorphous carbon substrate is not as good as the one in vacuum. In general, the wrapping of the MoS_2 layer on the tip of the Au nanorod is less continuous than along its facets. Figure 3a shows a STEM-

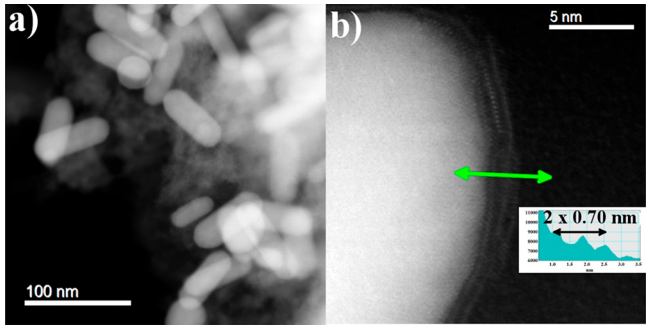

Figure 3. (a) STEM HAADF of an assortment of R-Au@MoS_2. (b) HR-STEM HAADF micrograph of the tip of a single R-Au@MoS_2 nanoparticle. The green arrow highlights the area used to extract the intensity profile, displayed in the inset, of the STEM HAADF image. The black arrow in the inset marks the distance between three peaks of the intensity profile, showing a 0.70 nm spacing between adjacent layers.

HAADF image of a group of R-Au@MoS_2. The average value of the aspect ratio is 2.5, with variation between 1.6 and 3.3. Figure 3b shows the tip of one such hybrid nanoparticle in greater detail. The individual MoS_2 layers are clearly discernible on the surface of the nanorod. The MoS_2 interlayer distance has been extracted from this image and is equal to 0.70 nm. This value is slightly higher than the one reported for the interlayer spacing of few-layer MoS_2 (0.62 nm).[38,39] The tip of the Au nanorod is coated with three MoS_2 layers, while two MoS_2 layers are seen at the facet of the nanorod. It is quite common to observe that the coating at the tip of the nanorod contains more MoS_2 layers than at the facets of the nanorods (Figure S4a). Note that the centers of the facets also tend to display a local increase of the number of MoS_2 layers (Figure S4b). Raman measurements of P-Au@MoS_2 and R-Au@MoS_2 showed that the separation of the E_{2g}^1 and A_{1g} peaks is 22−23 cm^{-1} and there is an observed shift of the E_{2g}^1 to lower frequencies (Figure S5). While a direct comparison with the literature is complex because of the somewhat different morphology of the samples, it is commonly accepted that a peak separation of less than 25 cm^{-1} corresponds to two to three molecular layers of MoS_2,[38] and the E_{2g}^1 shift is a fingerprint of S vacancies.[40−42]

3.1.3. Gold Nanostars Embedded within MoS_2 (S-Au@MoS_2). Large spiky nanostar Au particles were produced and coated with MoS_2. TEM images depict the nanostars before (Figure 4a−c) and after the coverage with MoS_2 (Figure 4d−f). The arm length varies between 60 and 360 nm, and the diameter of the entire nanostructure is in the range of 115−475 nm. The coverage on the Au nanostars was more amorphous (Figure 4f), since a thermal annealing stage resulted in the reconstruction of the Au particles into featureless structures and the loss of the spiky nature.

DOI: 10.1021/acsaem.9b01147
ACS Appl. Energy Mater. 2019, 2, 6043−6050

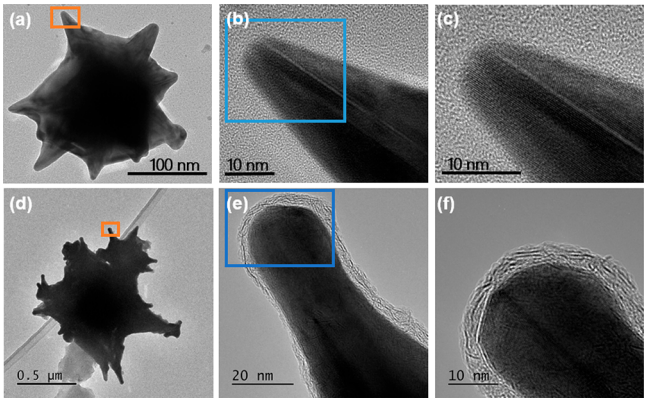

Figure 4. TEM images of Au nanostars. (a) Low-magnification image. (b) Higher magnification of the area in the orange frame marked in panel a. (c) Higher magnification of the area in the blue frame marked in panel b. TEM images of Au nanostars coated with MoS_2: S-Au@MoS_2. (d) Low-magnification image. (e) Higher magnification of the area in the orange frame marked in panel d. (f) Higher magnification of the area in the blue frame marked in panel e.

Additional data, including the change in absorption spectrum upon MoS_2 deposition, the powder XRD diffraction of the samples, and EDS chemical maps of the S-Au@MoS_2 structures are presented in Figures S6 and S7 in the Supporting Information.

3.2. Electrocatalytic Measurements. The electrocatalytic activity toward HER under acidic conditions (0.5 M H_2SO_4) was evaluated using a standard, three-electrode setup with the working electrode prepared by drop-casting the catalysts onto a polished glassy carbon (GC) electrode. The polarization curves are presented in Figure 5a from which we determine the overpotentials at 10 mA·cm^{-2} and the Tafel slopes (Figure 5b). The overpotentials of the hybrid materials are consistently lower than bare MoS_2 or Au. As reference samples, MoS_2 nanoflowers and Au-deposited nanoflowers were also prepared and measured for the catalytic activity toward HER (see the Supporting Information for detailed synthesis protocol and TEM images in Figure S8). The hybrids exhibit an improvement of more than 200 mV of the overpotential (at 10 mA·cm^{-2}) relative to edge-oriented MoS_2 nanoflowers, regardless of whether the Au particles are embedded within MoS_2 or exposed on its surface. The larger the Au structures, the lower is the overpotential at 10 mA·cm^{-2}, reaching 164 mV for S-Au@MoS_2. Interestingly, the structures with similar sizes of Au particles (P-Au@MoS_2 and nanoflowers deposited with Au particles) showed close results. The HER kinetics is also estimated using the corresponding Tafel plots (Figure 5b) from which we observe that MoS_2 nanoflowers or Au alone show inferior catalytic properties compared with the hybrid nanoparticles considering both the overpotential and the Tafel slope. The hybrid Au core−MoS_2 shell also shows substantially lower Tafel slopes, reaching 50 mV/dec for S-MoS_2, indicating a faster rate of the HER for the hybrids. The exchange current density, j_0, is presented in Table S1 and shows moderately higher values for the hybrids.

Additional insights into the improved catalytic activity of the hybrid Au@MoS_2 can be obtained via first-principles DFT calculations. In particular, we seek to understand, via DFT calculations, the relative importance of mechanical strains and electronic interactions that arise at the Au−MoS_2 core−shell interface, and the implications of these effects for the catalytic

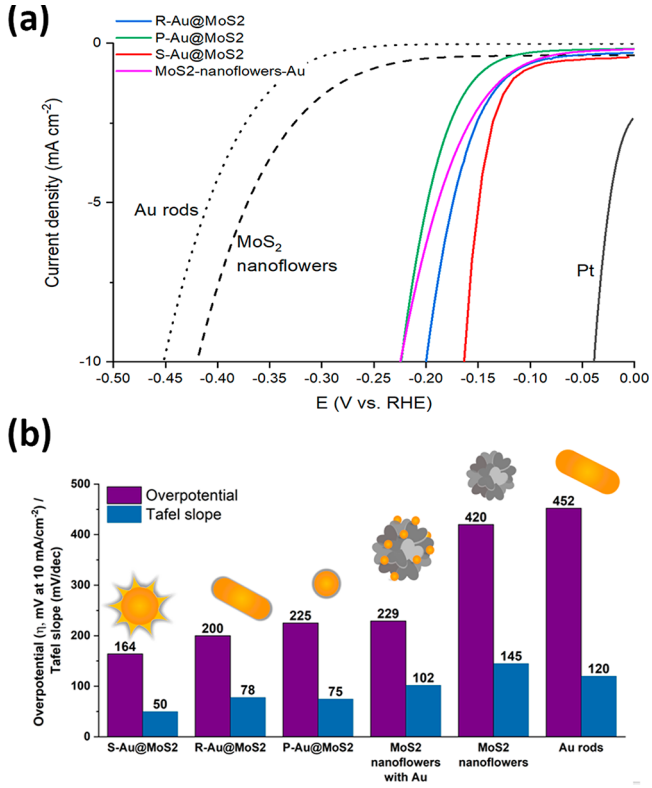

Figure 5. (a) HER polarization curves. The polarization curves are based on geometrical current density and not IR corrected. (b) Corresponding Tafel slopes obtained for the hybrid Au/MoS_2 materials, Au (bare rods), MoS_2 nanoflowers, and commercial 10% Pt/C in 0.5 M H_2SO_4 (pH ∼ 0.25). The scan rate of the polarization curves was 10 mV·s^{-1}.

properties of the MoS_2 shell. We modeled the Au@MoS_2 nanoparticle as a monolayer of MoS_2 (1L-MoS_2) supported on an Au(111) slab. As the calculated lattice mismatch between the MoS_2 monolayer and the Au surface is 7.72%, it is unrealistic to enforce epitaxial matching on the MoS_2 layer; the alternate approach of compressing the Au slab[34] leads to artifacts in the electronic structure of the support. While it is reasonable to expect some degree of tensile strain in the curved MoS_2 shell, the precise values for our samples are difficult to extract experimentally as some disorder of the MoS_2 shell is also expected, based on previous data.[43] Hence, we chose to model the supported hybrid Au/MoS_2 system by rotating the MoS_2 layer to produce two coincident-site lattices, one with a small biaxial tensile strain, ε = +0.67%, and the second with a larger tensile strain of ε = +2.48% (see the Supporting Information for more details). While it is not possible to account fully for the geometric complexity of the Au cores, the slab models employed here nevertheless allow us to explore separately the strain and support effects that influence the catalytic activity of the MoS_2 shell, thus allowing for broader conclusions beyond the specific set of Au core structures reported here.

Figure 6 displays the free energy of hydrogen adsorption (ΔG_H), a widely used descriptor of HER activity in acidic media,[44−46] for unsupported and Au-supported 1L-MoS_2 at standard conditions [300 K and a potential of 0 V vs reversible hydrogen electrode (RHE)]. ΔG_H was calculated as

DOI: 10.1021/acsaem.9b01147
ACS Appl. Energy Mater. 2019, 2, 6043−6050

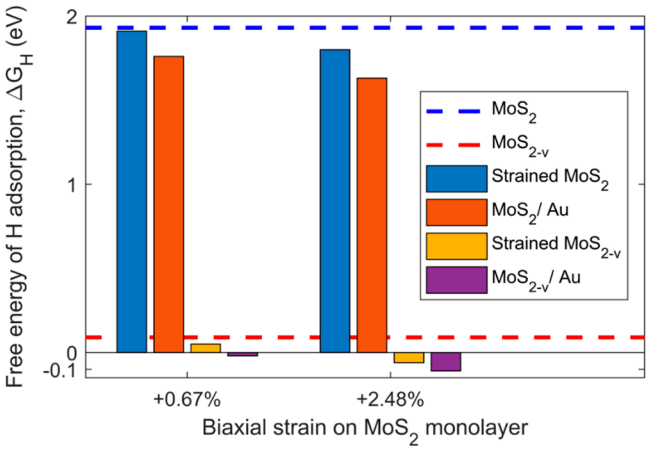

Figure 6. Free energy of H adsorption (ΔG_H) at S top sites and S-vacancy sites on the basal plane of freestanding MoS_2 monolayer and Au(111)-supported MoS_2 monolayer at biaxial tensile strains of +0.67% and +2.48%. MoS_2 and MoS_{2-v} represent the defect-free and defective single layers, respectively. Blue and red dashed lines are the reference values of ΔG_H at a S top site and a vacancy site, respectively, in the basal plane of an unstrained, freestanding MoS_2 monolayer.

$$\Delta G_H = E_{slab+H} - E_{slab} - \frac{E_{H_2}}{2} + \Delta E_{ZPE} - T\Delta S \quad (1)$$

where E_{slab+H}, E_{slab}, and E_{H_2} are the total energies of either 1L-MoS_2 or the composite 1L-MoS_2/Au(111) slab with an adsorbed H atom, the clean slab (no H), and an H_2 molecule in the gas phase, respectively; ΔE_{ZPE} and ΔS are the differences in zero-point energies and entropies, respectively, of an adsorbed H atom and its reference state in the H_2 molecule. As per Sabatier's principle,[47] a surface with $\Delta G_H = 0$ is an ideal HER catalyst[46] with negative/positive values of ΔG_H leading to over-/underbinding of H. In agreement with previous reports,[36,48−50] we find that the basal plane of the unstrained MoS_2 monolayer is inert toward HER due to its highly unfavorable $\Delta G_H \sim 1.9$ eV at a S top site. At +0.67% and +2.48% strain, the adsorption energy decreases by 0.02 and 0.13 eV, respectively; the addition of the Au(111) support further lowers ΔG_H by 0.15 eV (ε = +0.67%) and 0.16 eV (ε = +2.48%). While the electronic effect of the Au support is more significant than the strain effect, the resulting adsorption energies at the S top sites are still too thermodynamically unfavorable for HER. However, it is well-known that basal-plane S vacancies in MoS_2 are highly active for HER,[36,48] and indeed, we find that ΔG_H drops to ∼0.1 eV at a S-vacancy site in unstrained MoS_2 monolayer. At +0.67% and +2.48% strain, ΔG_H decreases slightly to 0.05 and −0.06 eV, respectively, and the addition of the Au support further reduces these adsorption energies to −0.02 and −0.11 eV. Thus, at low to moderate tensile strains, the support and strain effects act in synergy and render S-vacancy sites more favorable for HER.

Electronic structure calculations offer insights, beyond thermodynamic calculations, into the microscopic interactions between the MoS_2 monolayer and the Au(111) support. Figure 7 displays the total and angular-momentum-projected DOS of a pristine, unsupported MoS_2 monolayer and the Au-supported counterparts at +0.67% and +2.48% biaxial strains. The absence of electronic states near the Fermi level for unsupported MoS_2 monolayer renders H adsorption unfavorable, which is well-documented.[50] However, when an MoS_2 monolayer is deposited on an Au support, we notice the gradual emergence of gap states near the Fermi level, which leads to slightly stronger—albeit, still thermodynamically unfavorable—adsorption of H. The density of the gap states increases with increasing tensile strain, and the overall band-gap of MoS_2 also decreases as known from previous studies.[51−55] A Bader analysis[56−58] reveals that electrons are transferred from the Au slab to the MoS_2 monolayer (1.4×10^{13} e^-/cm^2 for ε = +0.67% and 8.28×10^{12} e^-/cm^2 for ε = +2.48%). Charge-density-difference plots (Figure 8) are consistent with the Bader analysis and reveal that charge redistribution occurs largely at the MoS_2/Au interface with smaller effects on the upper S basal plane.

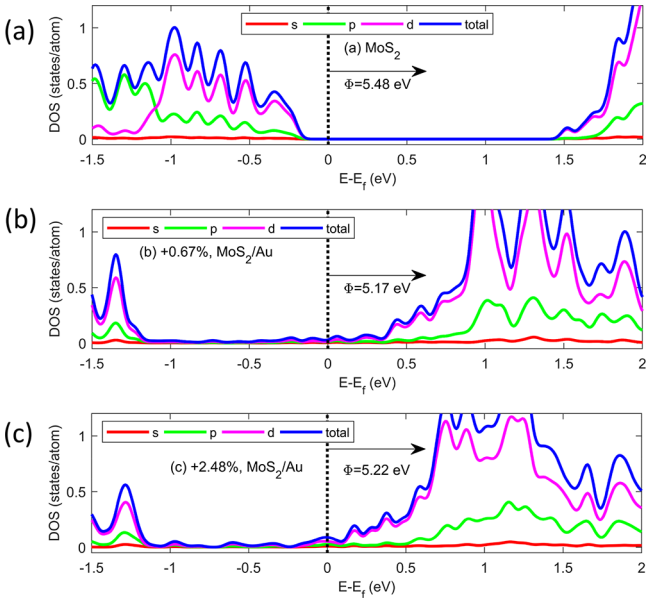

Figure 7. Total and angular-momentum-projected density-of-states (DOS) of (a) unsupported and unstrained 1L-MoS_2, (b) 1L-MoS_2 on Au(111) with +0.67% strain, and (c) 1L-MoS_2 on Au(111) with +2.48% strain. Only the states projected on to the MoS_2 layer are displayed for clarity, and the Au states are excluded. The Fermi level is set to zero, and the work function, Φ, of the various systems are also indicated in each panel.

For unstrained MoS_2 monolayer with vacancy defects (MoS_{2-v}; Figure 9), we find that dangling Mo bonds at the S vacancy appear as antibonding gap states, ∼1 eV above the Fermi level, consistent with previous reports[36,50,59] and these defect states are responsible for enhancing H adsorption. The addition of the Au support injects charge into the MoS_2 layer and shifts the Fermi level such that the vacancy defect states are much closer to the Fermi level, further stabilizing H adsorption at S-vacancy sites. Thus, our electronic structure studies confirm that, for a monolayer, the support effect, arising from charge transfer from Au to MoS_2, is dominant over the strain effect and that the new gap states introduced during this charge-transfer process are responsible for promoting H adsorption on the sulfur basal plane. Furthermore, charge transfer to the MoS_2 shell can also improve the conductivity of the semiconducting 2H phase, which is, in turn, beneficial for electrocatalysis. XPS measurements on P-Au@MoS_2 show a shift in the binding energies of the Mo toward lower binding energies (compared with pristine MoS_2) and a shift of the Au binding energies toward the higher energies, usually attributed

DOI: 10.1021/acsaem.9b01147
ACS Appl. Energy Mater. 2019, 2, 6043−6050

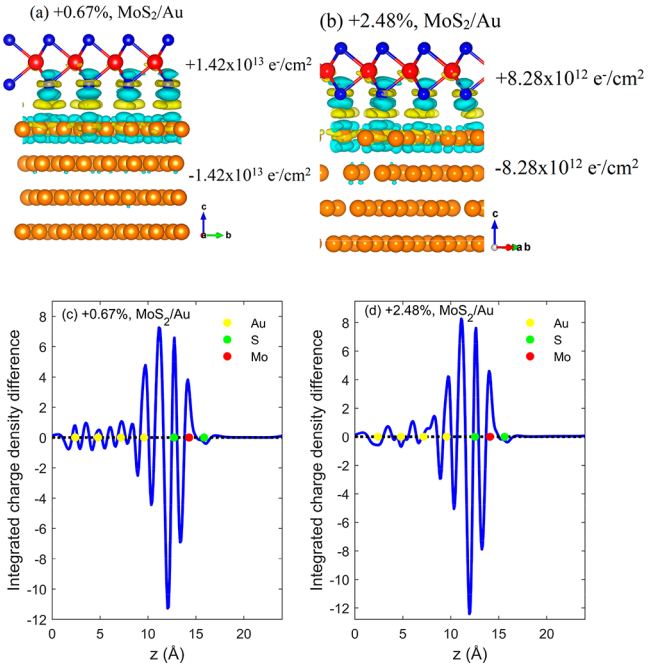

Figure 8. Charge-density-difference plots for MoS_2 on Au, at (a) +0.67% and (b) +2.48% strain. Isosurfaces are set to 4.4×10^{-3} and 5.7×10^{-3} $e^-/Å^3$ in panels a and b, respectively, and yellow/cyan colors indicate charge accumulation/depletion. The charge transferred from the Au slab to MoS_2 is indicated in each case. Blue, red, and orange spheres represent the S, Mo, and Au atoms. (c, d) Integrated (over *xy* plane) charge-density differences corresponding to panels a and b as a function of distance normal to the slab (*z*); yellow, green and red dots show the *z*-coordinates of Au, S, and Mo layers in the MoS_2/Au slab. Charge transfer is strongly localized at the MoS_2/Au interface.

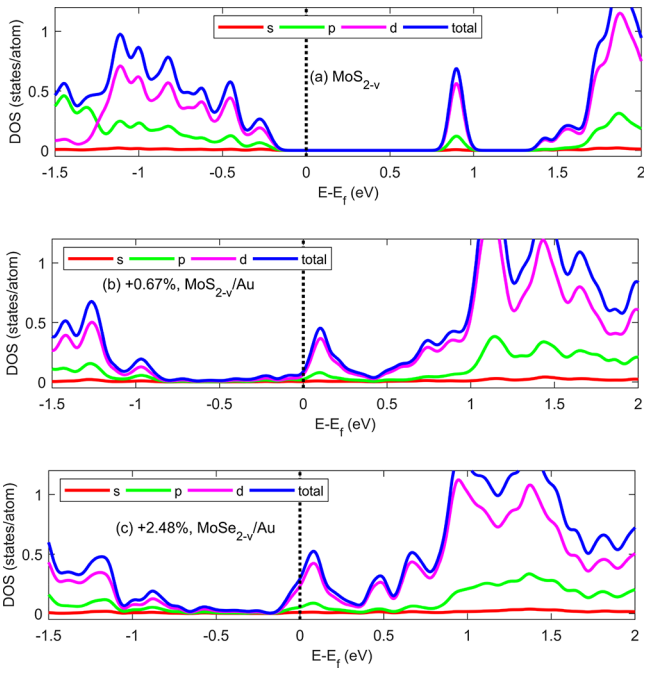

Figure 9. Total and angular-momentum-projected density-of-states of 1L-MoS_2 with a basal-plane S vacancy (MoS_{2-v}) for (a) an unsupported, unstrained single layer, (b) MoS_{2-v} on Au(111) at +0.67% strain, and (c) MoS_{2-v} on Au(111) at +2.48% strain.

to charge transfer from the Au to the Mo (see Figure S10 and Table S2 for the XPS data and analysis).

We also performed a more detailed analysis (see Supporting Information) of the competing thermodynamics of HER and electrochemical desulfurization, the latter having been shown to be a promising route for activation of MoS_2 via generation of sulfur vacancies.[45,60,61] In essence, the calculations show that, at negative potentials, the Au support not only stabilizes H adsorption at the catalytically active sites but also promotes the formation of basal-plane S vacancies in MoS_2. Tensile strains are slightly detrimental to the formation of vacancies, but once vacancies are formed, strain plays a smaller role in stabilizing H adsorption at these defects (see the Supporting Information). The insights gained from these trends may serve to explain the dominant factors in this system as well as to indicate further possible activation routes for these materials. In a nutshell, the MoS_2 shells are likely defect-rich, in order to encapsulate the Au nanoparticle, producing a combined effect whereby S vacancies, strain, and charge injection from the substrate all make the MoS_2 monolayer a better HER catalyst. Finally, while we have not modeled multilayer MoS_2@Au structures due to the computational cost, we expect that the improvement in HER activity will be less significant as compared to the monolayer case since the dominant charge-transfer effect is fairly localized to the interface between the first MoS_2 layer and the Au slab; the strain effect is expected to be of nearly similar magnitude between single and multiple layers and, as shown above, is of secondary importance to the charge-transfer effect.

4. CONCLUSIONS

In conclusion, we have presented a method to synthesize core−shell Au@MoS_2 nanoparticles and applied this to realize various MoS_2-coated Au nanoparticles. Electron microscopy showed that the MoS_2 layers completely encapsulate the Au nanoparticle even though these layers contain defects and seams. Such defects are more common near regions of high curvature such as the tips of the nanorods and nanostars. The hybrid Au@MoS_2 core−shell nanoparticles are superior electrocatalysts relative to freestanding MoS_2. Theoretical modeling suggests that the improved catalytic activity is likely due to charge transfer from the Au cores to the MoS_2 shells, which improves the electronic conductivity of the semiconducting MoS_2 shells and also reduces the energetic cost for generation of active chalcogen vacancy sites.

■ ASSOCIATED CONTENT

Supporting Information

The Supporting Information is available free of charge on the ACS Publications website at DOI: 10.1021/acsaem.9b01147.

Extended experimental section (including Materials and Methods); EELS measurements; additional TEM images; UV−vis absorption; EDS maps; XPS and Raman characterization; calculation of the exchange current density; theoretical modeling of the thermodynamics of HER versus electrochemical desulfurization; structural models of Au-supported MoS_2 monolayers (PDF)

■ AUTHOR INFORMATION

Corresponding Authors

*(M.B.-S.) E-mail: barsadan@bgu.ac.il.

DOI: 10.1021/acsaem.9b01147
ACS Appl. Energy Mater. 2019, 2, 6043−6050

*(L.L.) E-mail: luc.lajaunie@uca.es.
*(A.R.) E-mail: ashwin@engin.umass.edu.

ORCID

Ronen Bar-Ziv: 0000-0003-3082-7845
Reshef Tenne: 0000-0003-4071-0325
Raul Arenal: 0000-0002-2071-9093
Ashwin Ramasubramaniam: 0000-0001-6595-7442
Luc Lajaunie: 0000-0001-6152-6784
Maya Bar-Sadan: 0000-0002-1956-8195

Present Addresses

▲S.G.: Department of Chemistry, NIT Tiruchirappalli, TN-620015, India
◆Departamento de Ciencia de los Materiales e Ingeniería Metalúrgica y Química Inorgánica, Facultad de Ciencias, Universidad de Cádiz, Campus Río San Pedro S/N, Puerto Real 11510, Cádiz, Spain.

Notes

The authors declare no competing financial interest.

■ ACKNOWLEDGMENTS

The electron microscopy was performed at the Irving and Cherna Moscowitz Center for Nano and Bio-Nano Imaging of the Weizmann Institute of Science. We acknowledge the support of the Israel Science Foundation Grant No. 339/18; the Kimmel Center for Nanoscale Science Grant No. 43535000350000; the Irving and Azelle Waltcher Foundations in honor of Prof. M. Levy Grant No. 720821; and The Perlman Family Foundation. The HR-STEM and STEM-EELS studies were conducted at the Laboratorio de Microscopias Avanzadas, Universidad de Zaragoza, Spain. R.A. acknowledges support from Spanish MINECO Grant No. MAT2016-79776-P (AEI/FEDER, UE) and from EU H2020 "Graphene Flagship" Grant Agreement 785219. A.J. and A.R. gratefully acknowledge research funding from the U.S. Department of Energy under Award No. DE-SC0010610 and computing support from the Massachusetts Green High-Performance Computing Center. This research was supported by a grant from the United States−Israel Binational Science Foundation (BSF), Jerusalem, Israel (2016/149).

■ REFERENCES

(1) Asadi, M.; Kim, K.; Liu, C.; Addepalli, A. V.; Abbasi, P.; Yasaei, P.; Phillips, P.; Behranginia, A.; Cerrato, J. M.; Haasch, R.; Zapol, P.; Kumar, B.; Klie, R. F.; Abiade, J.; Curtiss, L. A.; Salehi-Khojin, A. Nanostructured transition metal dichalcogenide electrocatalysts for CO_2 reduction in ionic liquid. *Science* **2016**, *353* (6298), 467−470.
(2) Meiron, O. E.; Kuraganti, V.; Hod, I.; Bar-Ziv, R.; Bar-Sadan, M. Improved catalytic activity of $Mo_{1-x}W_xSe_2$ alloy nanoflowers promotes efficient hydrogen evolution reaction in both acidic and alkaline aqueous solutions. *Nanoscale* **2017**, *9* (37), 13998−14005.
(3) Vasu, K.; Meiron, O. E.; Enyashin, A. N.; Bar-Ziv, R.; Bar-Sadan, M. Effect of Ru Doping on the Properties of $MoSe_2$ Nanoflowers. *J. Phys. Chem. C* **2019**, *123* (3), 1987−1994.
(4) Li, G.; Zhang, D.; Qiao, Q.; Yu, Y.; Peterson, D.; Zafar, A.; Kumar, R.; Curtarolo, S.; Hunte, F.; Shannon, S.; Zhu, Y.; Yang, W.; Cao, L. All The Catalytic Active Sites of MoS_2 for Hydrogen Evolution. *J. Am. Chem. Soc.* **2016**, *138* (51), 16632−16638.
(5) Lukowski, M. A.; Daniel, A. S.; Meng, F.; Forticaux, A.; Li, L.; Jin, S. Enhanced Hydrogen Evolution Catalysis from Chemically Exfoliated Metallic MoS_2 Nanosheets. *J. Am. Chem. Soc.* **2013**, *135* (28), 10274−10277.
(6) Wilson, J. A.; Yoffe, A. D. The transition metal dichalcogenides discussion and interpretation of the observed optical, electrical and structural properties. *Adv. Phys.* **1969**, *18* (73), 193−335.
(7) Lin, Z.; Carvalho, B. R; Kahn, E.; Lv, R.; Rao, R.; Terrones, H.; Pimenta, M. A; Terrones, M. Defect engineering of two-dimensional transition metal dichalcogenides. *2D Mater.* **2016**, *3* (2), 022002.
(8) Xie, J.; Zhang, H.; Li, S.; Wang, R.; Sun, X.; Zhou, M.; Zhou, J.; Lou, X. W.; Xie, Y. Defect-Rich MoS_2 Ultrathin Nanosheets with Additional Active Edge Sites for Enhanced Electrocatalytic Hydrogen Evolution. *Adv. Mater.* **2013**, *25* (40), 5807−5813.
(9) Ye, G.; Gong, Y.; Lin, J.; Li, B.; He, Y.; Pantelides, S. T.; Zhou, W.; Vajtai, R.; Ajayan, P. M. Defects Engineered Monolayer MoS_2 for Improved Hydrogen Evolution Reaction. *Nano Lett.* **2016**, *16* (2), 1097−1103.
(10) Deng, J.; Li, H.; Xiao, J.; Tu, Y.; Deng, D.; Yang, H.; Tian, H.; Li, J.; Ren, P.; Bao, X. Triggering the Electrocatalytic Hydrogen Evolution Activity of the Inert Two-Dimensional MoS_2 Surface via Single-Atom Metal Doping. *Energy Environ. Sci.* **2015**, *8* (5), 1594−1601.
(11) Wang, H.; Zhang, Q.; Yao, H.; Liang, Z.; Lee, H.-W.; Hsu, P.-C.; Zheng, G.; Cui, Y. High Electrochemical Selectivity of Edge versus Terrace Sites in Two-Dimensional Layered MoS_2 Materials. *Nano Lett.* **2014**, *14* (12), 7138−7144.
(12) Li, Y.; Majewski, M. B.; Islam, S. M.; Hao, S.; Murthy, A. A.; DiStefano, J. G.; Hanson, E. D.; Xu, Y.; Wolverton, C.; Kanatzidis, M. G.; Wasielewski, M. R.; Chen, X.; Dravid, V. P. Morphological Engineering of Winged Au@MoS_2 Heterostructures for Electrocatalytic Hydrogen Evolution. *Nano Lett.* **2018**, *18* (11), 7104−7110.
(13) Maiti, P. S.; Ganai, A. K.; Bar-Ziv, R.; Enyashin, A. N.; Houben, L.; Bar Sadan, M. $Cu_{2-x}S$−MoS_2 Nano-Octahedra at the Atomic Scale: Using a Template To Activate the Basal Plane of MoS_2 for Hydrogen Production. *Chem. Mater.* **2018**, *30* (14), 4489−4492.
(14) Li, Y.; Cain, J. D.; Hanson, E. D.; Murthy, A. A.; Hao, S.; Shi, F.; Li, Q.; Wolverton, C.; Chen, X.; Dravid, V. P. Au@MoS_2 Core−Shell Heterostructures with Strong Light−Matter Interactions. *Nano Lett.* **2016**, *16* (12), 7696−7702.
(15) Li, Y.; DiStefano, J. G.; Murthy, A. A.; Cain, J. D.; Hanson, E. D.; Li, Q.; Castro, F. C.; Chen, X.; Dravid, V. P. Superior Plasmonic Photodetectors Based on Au@MoS_2 Core−Shell Heterostructures. *ACS Nano* **2017**, *11* (10), 10321−10329.
(16) Yu, Y.; Huang, S.-Y.; Li, Y.; Steinmann, S. N.; Yang, W.; Cao, L. Layer-Dependent Electrocatalysis of MoS_2 for Hydrogen Evolution. *Nano Lett.* **2014**, *14* (2), 553−558.
(17) Lavie, A.; Yadgarov, L.; Houben, L.; Popovitz-Biro, R.; Shaul, T.-E.; Nagler, A.; Suchowski, H.; Tenne, R. Synthesis of core−shell single-layer MoS_2 sheathing gold nanoparticles, AuNP@1L-MoS_2. *Nanotechnology* **2017**, *28* (24), 24LT03.
(18) DiStefano, J. G.; Li, Y.; Jung, H. J.; Hao, S.; Murthy, A. A.; Zhang, X.; Wolverton, C.; Dravid, V. P. Nanoparticle@MoS_2 Core−Shell Architecture: Role of the Core Material. *Chem. Mater.* **2018**, *30* (14), 4675−4682.
(19) Li, Z.; Jiang, S.; Xu, S.; Zhang, C.; Qiu, H.; Li, C.; Sheng, Y.; Huo, Y.; Yang, C.; Man, B. Few-layer MoS_2-encapsulated Cu nanoparticle hybrids fabricated by two-step annealing process for surface enhanced Raman scattering. *Sens. Actuators, B* **2016**, *230*, 645−652.
(20) Chen, P. X.; Qiu, H. W.; Xu, S. C.; Liu, X. Y.; Li, Z.; Hu, L. T.; Li, C. H.; Guo, J.; Jiang, S. Z.; Huo, Y. Y. A novel surface-enhanced Raman spectroscopy substrate based on a large area of MoS_2 and Ag nanoparticles hybrid system. *Appl. Surf. Sci.* **2016**, *375*, 207−214.
(21) Eustis, S.; El-Sayed, M. A. Why gold nanoparticles are more precious than pretty gold: Noble metal surface plasmon resonance and its enhancement of the radiative and nonradiative properties of nanocrystals of different shapes. *Chem. Soc. Rev.* **2006**, *35* (3), 209−217.
(22) Shi, Y.; Wang, J.; Wang, C.; Zhai, T.-T.; Bao, W.-J.; Xu, J.-J.; Xia, X.-H.; Chen, H.-Y. Hot Electron of Au Nanorods Activates the Electrocatalysis of Hydrogen Evolution on MoS_2 Nanosheets. *J. Am. Chem. Soc.* **2015**, *137* (23), 7365−7370.

DOI: 10.1021/acsaem.9b01147
ACS Appl. Energy Mater. 2019, 2, 6043−6050

(23) Yin, Z.; Chen, B.; Bosman, M.; Cao, X.; Chen, J.; Zheng, B.; Zhang, H. Au Nanoparticle-Modified MoS_2 Nanosheet-Based Photoelectrochemical Cells for Water Splitting. *Small* **2014**, *10* (17), 3537−3543.
(24) Li, X.; Guo, S.; Kan, C.; Zhu, J.; Tong, T.; Ke, S.; Choy, W. C. H.; Wei, B. Au Multimer@MoS_2 hybrid structures for efficient photocatalytical hydrogen production via strongly plasmonic coupling effect. *Nano Energy* **2016**, *30* (C), 549−558.
(25) Yang, L.; Guo, S.; Li, X. Au nanoparticles@MoS_2 core-shell structures with moderate MoS_2 coverage for efficient photocatalytic water splitting. *J. Alloys Compd.* **2017**, *706*, 82−88.
(26) Shi, J.; Ma, D.; Han, G.-F.; Zhang, Y.; Ji, Q.; Gao, T.; Sun, J.; Song, X.; Li, C.; Zhang, Y.; Lang, X.-Y.; Zhang, Y.; Liu, Z. Controllable Growth and Transfer of Monolayer MoS_2 on Au Foils and Its Potential Application in Hydrogen Evolution Reaction. *ACS Nano* **2014**, *8* (10), 10196−10204.
(27) Sivan, Y.; Un, I. W.; Dubi, Y. Assistance of metal nanoparticles in photocatalysis − nothing more than a classical heat source. *Faraday Discuss.* **2019**, *214*, 215−233.
(28) Kresse, G.; Furthmüller, J. Efficient iterative schemes for ab initio total-energy calculations using a plane-wave basis set. *Phys. Rev. B: Condens. Matter Mater. Phys.* **1996**, *54* (16), 11169−11186.
(29) Kresse, G.; Furthmüller, J. Efficiency of ab-initio total energy calculations for metals and semiconductors using a plane-wave basis set. *Comput. Mater. Sci.* **1996**, *6* (1), 15−50.
(30) Blöchl, P. E. Projector Augmented-Wave Method. *Phys. Rev. B: Condens. Matter Mater. Phys.* **1994**, *50* (24), 17953−17979.
(31) Kresse, G.; Joubert, D. From ultrasoft pseudopotentials to the projector augmented-wave method. *Phys. Rev. B: Condens. Matter Mater. Phys.* **1999**, *59* (3), 1758−1775.
(32) Perdew, J. P.; Burke, K.; Ernzerhof, M. Generalized Gradient Approximation Made Simple. *Phys. Rev. Lett.* **1996**, *77* (18), 3865−3868.
(33) Makov, G.; Payne, M. C. Periodic boundary conditions in ab initio calculations. *Phys. Rev. B: Condens. Matter Mater. Phys.* **1995**, *51* (7), 4014−4022.
(34) Neugebauer, J.; Scheffler, M. Adsorbate-substrate and adsorbate-adsorbate interactions of Na and K adlayers on Al(111). *Phys. Rev. B: Condens. Matter Mater. Phys.* **1992**, *46* (24), 16067−16080.
(35) Tsai, C.; Chan, K.; Nørskov, J. K.; Abild-Pedersen, F. Theoretical insights into the hydrogen evolution activity of layered transition metal dichalcogenides. *Surf. Sci.* **2015**, *640*, 133−140.
(36) Li, H.; Tsai, C.; Koh, A. L.; Cai, L.; Contryman, A. W.; Fragapane, A. H.; Zhao, J.; Han, H. S.; Manoharan, H. C.; Abild-Pedersen, F.; Nørskov, J. K.; Zheng, X. Activating and optimizing MoS_2 basal planes for hydrogen evolution through the formation of strained sulphur vacancies. *Nat. Mater.* **2016**, *15*, 48.
(37) Stadelmann, P. *JEMS-SAAS*, ems java version V4; 2014; http://www.jems-saas.ch/Home/jemsWebSite/jems.html.
(38) Lee, C.; Yan, H.; Brus, L. E.; Heinz, T. F.; Hone, J.; Ryu, S. Anomalous Lattice Vibrations of Single- and Few-Layer MoS_2. *ACS Nano* **2010**, *4* (5), 2695−2700.
(39) Deokar, G.; Vignaud, D.; Arenal, R.; Louette, P.; Colomer, J. F. Synthesis and characterization of MoS_2 nanosheets. *Nanotechnology* **2016**, *27* (7), 075604.
(40) Parkin, W. M.; Balan, A.; Liang, L.; Das, P. M.; Lamparski, M.; Naylor, C. H.; Rodríguez-Manzo, J. A.; Johnson, A. T. C.; Meunier, V.; Drndić, M. Raman Shifts in Electron-Irradiated Monolayer MoS_2. *ACS Nano* **2016**, *10* (4), 4134−4142.
(41) Chen, Y.; Huang, S.; Ji, X.; Adepalli, K.; Yin, K.; Ling, X.; Wang, X.; Xue, J.; Dresselhaus, M.; Kong, J.; Yildiz, B. Tuning Electronic Structure of Single Layer MoS_2 through Defect and Interface Engineering. *ACS Nano* **2018**, *12* (3), 2569−2579.
(42) Wu, K.; Li, Z.; Tang, J.; Lv, X.; Wang, H.; Luo, R.; Liu, P.; Qian, L.; Zhang, S.; Yuan, S. Controllable defects implantation in MoS_2 grown by chemical vapor deposition for photoluminescence enhancement. *Nano Res.* **2018**, *11* (8), 4123−4132.
(43) Gołasa, K.; Grzeszczyk, M.; Binder, J.; Bożek, R.; Wysmołek, A.; Babiński, A. The disorder-induced Raman scattering in Au/MoS_2 heterostructures. *AIP Adv.* **2015**, *5* (7), 077120.
(44) Greeley, J.; Jaramillo, T. F.; Bonde, J.; Chorkendorff, I.; Nørskov, J. K. Computational high-throughput screening of electrocatalytic materials for hydrogen evolution. *Nat. Mater.* **2006**, *5*, 909.
(45) Norskov, J. K.; Bligaard, T.; Logadottir, A.; Kitchin, J. R.; Chen, J. G.; Pandelov, S.; Stimming, U. Trends in the exchange current for hydrogen evolution. *J. Electrochem. Soc.* **2005**, *152* (3), J23−J26.
(46) Parsons, R. The rate of electrolytic hydrogen evolution and the heat of adsorption of hydrogen. *Trans. Faraday Soc.* **1958**, *54* (0), 1053−1063.
(47) Sabatier, P. *Catalysis in Organic Chemistry*. D. Van Nostrand: New York, 1922.
(48) Tsai, C.; Li, H.; Park, S.; Park, J.; Han, H. S.; Nørskov, J. K.; Zheng, X.; Abild-Pedersen, F. Electrochemical generation of sulfur vacancies in the basal plane of MoS_2 for hydrogen evolution. *Nat. Commun.* **2017**, *8*, 15113.
(49) Jin, H.; Guo, C.; Liu, X.; Liu, J.; Vasileff, A.; Jiao, Y.; Zheng, Y.; Qiao, S.-Z. Emerging Two-Dimensional Nanomaterials for Electrocatalysis. *Chem. Rev.* **2018**, *118* (13), 6337−6408.
(50) Lin, S.-H.; Kuo, J.-L. Activating and tuning basal planes of MoO_2, MoS_2, and $MoSe_2$ for hydrogen evolution reaction. *Phys. Chem. Chem. Phys.* **2015**, *17* (43), 29305−29310.
(51) He, K.; Poole, C.; Mak, K. F.; Shan, J. Experimental Demonstration of Continuous Electronic Structure Tuning via Strain in Atomically Thin MoS_2. *Nano Lett.* **2013**, *13* (6), 2931−2936.
(52) Conley, H. J.; Wang, B.; Ziegler, J. I.; Haglund, R. F.; Pantelides, S. T.; Bolotin, K. I. Bandgap Engineering of Strained Monolayer and Bilayer MoS_2. *Nano Lett.* **2013**, *13* (8), 3626−3630.
(53) Scalise, E.; Houssa, M.; Pourtois, G.; Afanas'ev, V.; Stesmans, A. Strain-induced semiconductor to metal transition in the two-dimensional honeycomb structure of MoS_2. *Nano Res.* **2012**, *5* (1), 43−48.
(54) Johari, P.; Shenoy, V. B. Tuning the Electronic Properties of Semiconducting Transition Metal Dichalcogenides by Applying Mechanical Strains. *ACS Nano* **2012**, *6* (6), 5449−5456.
(55) Koskinen, P.; Fampiou, I.; Ramasubramaniam, A. Density-Functional Tight-Binding Simulations of Curvature-Controlled Layer Decoupling and Band-Gap Tuning in Bilayer MoS_2. *Phys. Rev. Lett.* **2014**, *112* (18), 186802.
(56) Henkelman, G.; Arnaldsson, A.; Jónsson, H. A fast and robust algorithm for Bader decomposition of charge density. *Comput. Mater. Sci.* **2006**, *36* (3), 354−360.
(57) Sanville, E.; Kenny, S. D.; Smith, R.; Henkelman, G. Improved grid-based algorithm for Bader charge allocation. *J. Comput. Chem.* **2007**, *28* (5), 899−908.
(58) Tang, W.; Sanville, E.; Henkelman, G. A grid-based Bader analysis algorithm without lattice bias. *J. Phys.: Condens. Matter* **2009**, *21* (8), 084204.
(59) Le, D.; Rawal, T. B.; Rahman, T. S. Single-Layer MoS_2 with Sulfur Vacancies: Structure and Catalytic Application. *J. Phys. Chem. C* **2014**, *118* (10), 5346−5351.
(60) Park, S.; Park, J.; Abroshan, H.; Zhang, L.; Kim, J. K.; Zhang, J.; Guo, J.; Siahrostami, S.; Zheng, X. Enhancing Catalytic Activity of MoS_2 Basal Plane S-Vacancy by Co Cluster Addition. *ACS Energy Lett.* **2018**, *3* (11), 2685−2693.
(61) Li, G.; Fu, C.; Wu, J.; Rao, J.; Liou, S.-C.; Xu, X.; Shao, B.; Liu, K.; Liu, E.; Kumar, N.; Liu, X.; Fahlman, M.; Gooth, J.; Auffermann, G.; Sun, Y.; Felser, C.; Zhang, B. Synergistically creating sulfur vacancies in semimetal-supported amorphous MoS_2 for efficient hydrogen evolution. *Appl. Catal., B* **2019**, *254*, 1−6.

DOI: 10.1021/acsaem.9b01147
ACS Appl. Energy Mater. 2019, 2, 6043−6050